RESTORATION OF MRI DATA FOR INTENSITY NON-UNIFORMITIES USING LOCAL HIGH ORDER INTENSITY STATISTICS

Stathis Hadjidemetriou[a], Colin Studholme[b], Susanne Mueller[b], Michael Weiner[b], and Norbert Schuff[b]

[a]NCIRE/VA UCSF, 4150 Clement St., San Francisco, CA 94121,
[b]UCSF, 4150 Clement St., San Francisco, CA 94121

ABSTRACT

MRI at high magnetic fields ($> 3.0T$) is complicated by strong inhomogeneous radio-frequency fields, sometimes termed the "bias field". These lead to non-biological intensity non-uniformities across the imaged brain. They can complicate further analysis such as registration and tissue segmentation. Existing methods for intensity uniformity restoration have been optimized for $1.5T$, but they are less effective for $3.0T$ MRI, and not at all satisfactory for higher fields. Also, many of the existing restoration algorithms require a brain template or use a prior atlas, which can restrict their practicalities. This paper develops an effective intensity uniformity restoration algorithm based on non-parametric statistics of high order local intensity co-occurrences. These statistics are restored with a non-stationary Weiner filter. The algorithm also assumes a smooth non-uniformity and is stable. It does not require a prior atlas and is robust to variations in anatomy. In geriatric brain imaging it is robust to variations such as enlarged ventricles, lesions, and low contrast to noise ratio. The co-occurrence statistics improve robustness to whole head images with pronounced non-uniformities present in high field acquisitions. Its significantly improved performance and efficiency has been demonstrated by comparing it to the very commonly used N3 algorithm on $1.5T$ MNI BrainWeb head phantoms and high field $4T$ human head images.

Keywords: Image intensity restoration, bias field correction, co-occurrence statistics, high order image statistics, non-stationary Weiner filtering.

1. INTRODUCTION

In-vivo human magnetic resonance imaging (MRI) is a non-invasive imaging technique that provides good quality volumetric datasets. It is used in clinical practice and research for studying anatomy and pathology such as brain injury and neurodegenerative diseases. Longitudinal MRI can also be used to monitor the progression of these conditions or their potential reversal with treatment. The qualitative interpretation of such data or the user-driven quantitative interpretation is very limited and cumbersome due to the data size. Qualitative analysis is also not reproducible. To take advantage of the imaging data the quantification must be done automatically.

The accurate acquisition of MRI data requires a homogeneous radio-frequency field, which is not possible to achieve. The inhomogeneity is sometimes termed the "bias field". The non-uniform radio-frequency field results in non-biological intensity non-uniformities across the imaged brain. While a new generation of high-field MRI scanners ($> 3.0T$) has significantly improved the resolution of MR imaging, it suffers from more pronounced intensity non-uniformities. In high fields the radio-frequency wavelength gets shorter, approaching the dimension of the human head or body [1]. The local dielectric properties of these regions lead to non-uniformity of image intensity, greatly complicating further analysis such as registration and tissue segmentation.

Corresponding author: Email: efstathios.hadjidemetriou@ucsf.edu, Phone: 415-221-4810 ext. 4801, Fax:415-668-2864.

There have been several attempts to correct for non-uniformity during acquisition based on its physical properties. The non-uniformity of the transmission coil has been estimated from its frequency response to parameterized acquisition sequences [2, 3]. In addition, the non-uniformity of transmission and receiver coil(s) combined has been approximated using phantoms [4]. However, the physical correction methods are valid only for a particular MRI sequence and do not account for the complicated interaction between the radio-frequency fields and the human body. It is not obvious how the combined non-uniformities can be accounted for during acquisition, especially for higher magnetic fields. Thus, existing methods for correction of the non-uniformities during acquisition are incomplete, time consuming, and clinically impractical.

As an alternative to physical corrections, several post-acquisition restoration methods have been proposed to account for the effect of non-uniformities that do not require additional acquisitions and are applicable to a range of MRI sequences [5, 6, 7, 8]. They make regularity assumptions about the field non-uniformity as well as anatomy and treat the non-uniformities in the same way irrespective of their sources. Typically, they operate on the logarithm of image intensities [9, 10, 11] and assume that the non-uniformity can be approximated by basis functions such as Gaussians, splines, polynomials, or sinusoids. Existing methods for intensity uniformity restoration have been optimized for $1.5T$ images, but they are less effective for $3.0T$ MRI, and not at all satisfactory for higher fields. The simplest approach to address this problem has been homomorphic filtering [12, 13]. This is based on the assumption that the non-uniformity corresponds to spatial frequencies lower than those of the anatomy. Thus, the non-uniformity is obtained by smoothing an image in the spatial or frequency domain. Smoothing has also been applied to statistics of local histograms computed over image tiles [12, 14]. The basic assumption of homomorphic filtering, that the spatial frequencies of the non-uniformity are lower than those of the anatomy, can be problematic for high field MR images. In such images the non-uniformity can extend from the low frequency part of their spectrum until the intermediate frequency range.

Another class of approaches estimates non-uniformity by registering the data to tissue templates or an atlas and by using these directly [15] or as priors for subsequent processing [10, 16]. Non-uniformity estimation has also been combined with tissue classification. Such approaches require initialization with manual presegmentation [17, 18, 19, 20] while others are automatic [21, 22]. Some of these approaches estimate tissue classification based on expectation maximization [23] over the histogram [18, 19, 20, 24], or fuzzy c-means classification [25, 26]. Intensity tissue classification has also been enhanced by breaking an image into subregions [27, 28] and using spatial Markov random fields [18, 19, 20, 9, 10, 11]. Estimating the non-uniformity with registration and tissue segmentation depends extensively on the prior assumptions. The accuracy of registration is affected when the image has a pronounced non-uniformity such as that present in $> 3T$ images. This poses a problem when registration is used to extract the brain region from a head image in preprocessing. Also the priors of an algorithm may be unable to represent the intensity variations of anatomy or pathology in the data. Moreover, there may not be adequate contrast between the assumed tissue classes.

Several non-parametric approaches have been suggested that are more robust to inter and intra subject variability as well as pathology. One such class of non-parametric techniques is based on the retinex algorithm [29, 30, 31]. This algorithm uses the logarithm of the intensities and normalizes them to the geometric mean of the intensities within a neighborhood. Thus, it enhances the components of the non-uniformity whose wavelengths are close to the size of the neighborhood considered and introduces overshooting contours at the borders between different tissue regions [30]. This problem can be alleviated but not resolved by using the multiresolution of an image in terms of a Gaussian or a more general wavelet representation [32, 31]. Another class of non-parametric approaches assume that the image is a piecewise union of extensive regions of constant intensity. These methods compute image derivatives such as the gradient or Laplacian and threshold their low values assumed to be due to non-uniformities exclusively. The remaining derivatives are incorporated into a regularized cost functional whose minimization estimates the non-uniformity [33, 34, 35]. The assumption of extensive homogeneous regions does not hold in many anatomical regions including the brain cortices, which are regions of great interest in a variety of clinical studies. Both retinex and variational methods operate locally and may not restore global image statistics. They

also assume a distinction between a low frequency non-uniformity and a high frequency anatomy. More generally, the use of differential image properties [36] may lead to restorations that depend on image structure rather than intensity non-uniformity.

Another class of non-parametric techniques uses directly the global image intensity histogram [37, 38]. These methods can capture global image properties. They assume that the non-uniformity widens the intensity distributions of the various tissues. Thus, the sharpening of the histogram is assumed to restore image intensity uniformity. This is achieved by estimating a smooth estimate of the non-uniformity. A non-parametric technique, N3 [38], was found to have a performance superior to those based on homomorphic filtering [5]. The ability of the intensity histogram to discriminate between different distributions affected by high fields is limited due to the corruption of the distributions caused by the spatial non-uniformity. A common sharpness optimality criterion for histogram based methods is minimum entropy, which corresponds to single peak histograms resulting from nearly flat images without anatomic information [37, 39, 40]. Thus, the direct use of entropy can be problematic in terminating an iterative numerical algorithm.

This paper develops a non-parametric approach for intensity uniformity restoration that is effective for high field MRI especially for brain imaging [41]. It is based on local high order intensity coincidence or co-occurrence statistics. Since it is non-parametric, it is robust to subject anatomy, pathology, and intensity variations within a tissue. The co-occurrence statistics represent the intensities of different tissues as well as the joint intensities of adjacent tissues. The high order of coincidences favors dominant distributions and selectively decrease the contribution of noise to their variance. The effect of the image intensity distortion on the co-occurrence statistics is modeled as a point spread function and used to design a non-stationary Weiner filter to restore the statistics. The algorithm is also based on the reasonable assumption that the non-uniformity is smoothly varying in space. The restoration algorithm is iterative with a robust stopping criterion based on the entropy of the co-occurrence distribution normalized with respect to the effective dynamic range, namely, the scaled entropy. This algorithm is able to perform intensity uniformity restoration for human head data acquired under high field with an emphasis on the brain region that gives rise to the dominant distributions of the white matter and of the region around the interface between white matter and gray matter. It was found to have a better performance than the commonly used N3 technique over the same data [38].

2. METHODS

The model of the image as well as the image restoration emphasize the intensity non-uniformity distortion. We assume that the intensity non-uniformity is spatially smooth. Thus, we do not consider image noise, which has high spatial frequencies. The restoration is iterative with a stable stopping criterion. An overview of the algorithm is sketched in figure 5.

2.1. Intensity Non-Uniformity Model

We assume that the measured image I and the true anatomic image I_A are related according to:

$$I = BI_A + N, \tag{1}$$

where matrix B contains the unknown non-uniformity field and the noise N is additive. The statistics of I_A are assumed to consist of distributions that can be discriminated. The Taylor series expansion of the non-uniformity around a voxel $\mathbf{x}_0$ gives:

$$B(\mathbf{x}) = B(\mathbf{x}_0) + \nabla B(\mathbf{x})|_{\mathbf{x}_0}(\mathbf{x} - \mathbf{x}_0) + O(\mathbf{x}^2). \tag{2}$$

Approximation up to the first order term leads to a non-uniformity which is locally linear within a sphere of radius $\rho = \mathbf{x} - \mathbf{x}_0$ around $\mathbf{x}_0$. Thus, quadratic and higher order terms are assumed to be negligible within distance ρ

from $\mathbf{x}_0$. The non-uniformity is recovered within a scale factor which does not affect the discriminability between tissues. We also assume that the noise N is Gaussian, stationary, and white [42].

2.2. Preprocessing for Selection of the Valid Intensity Range of an Image

The valid dynamic range of the MR contrast mechanism is detected and very bright artifacts due to instrumental imperfections or blood flow are removed since they do not follow the non-uniformity assumption of equation (1). To this end we compute the histogram h of the original image I and the cumulative histogram $\mathcal{H} = \int_u h du$. We compute the intensity value $u^{0.9}$ that corresponds to the upper 0.9 percentile of $\mathcal{H}$, $\mathcal{H}(u^{0.9}) = 0.9$. The intensity range up to $1.5 \times u^{0.9}$ is preserved, whereas the intensity range beyond that value is linearly compressed to the range $(1.5 \times u^{0.9}, 3.0 \times u^{0.9}]$ with maximum intensity $u_{max} = 3.0 \times u^{0.9}$ to provide an initial estimate of image I_0. The same intensity range $[0, u_{max}]$ is maintained during the iterations t. The domain of the image D is a subset of three-dimensional space $D \in \mathbf{x}$. The image is the map from its domain to its intensity range $I_t : D \rightarrow [0, u_{max}]$.

2.3. High Order Intensity Co-Occurrence Statistics

The statistics of image I_t used in this work are the nth-order co-occurrences of pairs of intensities within spherical neighborhoods of radius ρ, assuming that the non-uniformity field in spherical windows of this size is linear. The count of intensities in range $u \in [0, u_{max}]$ in a sphere of radius ρ around voxel $\mathbf{x}_0$ is given by:

$$h_t(\mathbf{x}_0, \rho, u) = \int_{I_t^{-1}(u) \cap |\mathbf{x} - \mathbf{x}_0| \leq \rho} d\mathbf{x}. \tag{3}$$

In an nth-order co-occurrence between intensity u_0 and intensity u_1 the center of the spherical neighborhood has intensity u_0 and the remaining window contains at least $n-1$ voxels of the same intensity and at least n voxels of intensity u_1. Additional voxels of any of the two intensities within the spherical window ρ give the co-occurrence:

$$c_t(\mathbf{x}_0, \rho, u_0, u_1) = \begin{cases} \max(h_t(\mathbf{x}_0, \rho, u_0) - n, 0) + \max(h_t(\mathbf{x}_0, \rho, u_1) - n, 0) & if \quad I_t(\mathbf{x}_0) = u_0 \cap \\ & \cap h_t(\mathbf{x}_0, u_0) \geqslant n \cap \\ & \cap h_t(\mathbf{x}_0, u_1) \geqslant n \\ 0 & otherwise, \end{cases} \tag{4}$$

where $c_t(\mathbf{x}_0, \rho, u_0, u_1)$ are the co-occurrences at $\mathbf{x}_0$ for radius ρ and iteration t. The image co-occurrences are given by integrating the intensity co-occurrences over the entire image domain. The co-occurrence statistics are computed with a two dimensional Gaussian Parzen window $G(\sigma_c)$ to give the probability distribution:

$$C_t(\rho, u_0, u_1) = \int_D c_t(\mathbf{x}, \rho, u_0, u_1) G(\sigma_c) d\mathbf{x}, \tag{5}$$

which is a 2D matrix. This is the joint intensity distribution of nth-order of an image with itself computed within spheres of radius ρ. The resulting matrix C_t is not necessarily symmetric for high order co-occurrences $n > 1$. The co-occurrences in a region with a contiguous tissue lie close to the diagonal of matrix C_t. The joint co-occurrences of tissues around an interface of different tissues lie farther from the diagonal. To examine the properties of the co-occurrence matrix we assume that the distributions of I_A in the co-occurrence statistics C_A are Gaussian. In appendix 5.1 it is shown that regions of contiguous tissue have co-occurrence statistics whose variance is lower than the statistics of the same region in the histogram.

2.4. Effect of Image Distortion on Co-Occurrence Statistics

Figure 1 shows the effects of some types of image intensity distortions on the co-occurrence statistics using BrainWeb T1 phantom images [43, 44]. In the first row is the true uncorrupted T1 phantom image. The distributions in its co-occurrence matrix are sharp. The horizontal and vertical streaks are caused by the partial volume artifact. The second row shows an image without intensity non-uniformity, but with high Gaussian noise $N = 5\%$. The distributions in its co-occurrence matrix are Gaussians. The presence of additive zero mean Gaussian noise N in an image increases the variances of the distributions in the statistics C of the image. The third row in figure 1 shows a phantom with limited noise $N = 3\%$ and high intensity non-uniformity $B = 40\%$. The effect of the non-uniformity is primarily to elongate the distributions along lines passing from the origin.

Image intensity non-uniformity affects intensity co-occurrences between u_0 and u_1 where u_0 is the intensity of the central voxel at $\mathbf{x}_0$ in a hypothetical anatomic image I_A. The effect is to scale and rotate them about the origin of C_{I_A}. The zero order term $B(\mathbf{x}_0)$ in equation (2) scales co-occurrences around the origin. The first order term $\nabla B(\mathbf{x}_0)$ in equation (2) rotates them around the origin. The geometry of the angular distortion in the statistics is demonstrated in figure 9 (a). The effect of the non-uniformity on co-occurrence statistics C is simpler to examine in polar coordinates (r, ϕ), where $r = \sqrt{u_0^2 + u_1^2}$ and $\tan\phi = u_1/u_0$. We assume that the effect of the non-uniformity B on the co-occurrence statistics of the true image C_{I_A} is a Gaussian point spread function both along the radial dimension r and the angular dimension ϕ. The co-occurrence statistics of the initial image C_{I_0} are also assumed to be corrupted by additive Gaussian noise N_C. Thus, the effect of the image distortion in equation (1) on the co-occurrence statistics is given by $C_{I_0} = C_{I_A} * G(\sigma_r) * G(\sigma_\phi) + N_C$, where σ_r is the radial standard deviation of the point spread function, and σ_ϕ is the angular standard deviation of the point spread function.

The standard deviation σ_r of the radial point spread function $G(\sigma_r)$ depends on the mean value of the non-uniformity, $\overline{B(\mathbf{x}_0)}$. It is shown in appendix 5.2 to be:

$$\sigma_r \propto \overline{B(\mathbf{x}_0)} r. \tag{6}$$

The standard deviation σ_ϕ of the angular point spread function $G(\sigma_\phi)$ depends on the mean value of the gradient of the non-uniformity, $\mu_{\nabla B} = \overline{\nabla B(\mathbf{x}_0)}$. It is shown in appendix 5.3 to be:

$$\sigma_\phi = 2\sin^{-1}\left[\frac{1}{\sqrt{2}}\sqrt{1 - \frac{1 + \tan^2\phi(1 + \mu_{\nabla B})}{\sqrt{(1 + \tan^2\phi)(1 + \tan^2\phi(1 + \mu_{\nabla B})^2)}}}\right]. \tag{7}$$

This relation is plotted in figure 9 (b).

2.5. Restoration of the Co-Occurrence Statistics for Image Intensity Uniformity

To product in equation (1) is decomposed to estimate I_t as well as a smooth B_t using the co-occurrence statistics. The effect that the non-uniformity B_t has on C_t is unmixed, where B_t is the estimate of B at iteration t. To unmix the effect of the non-uniformity we use the point spread functions of the distortion whose statistics are given by equation (6) and equation (7). They are used to compute the non-stationary Weiner restoration filters for the statistics. The radial and angular restoration filters are

$$f_r = \frac{G(\sigma_r)}{\|G(\sigma_r)\|_2^2 + \epsilon}, \quad \text{and} \quad f_\phi = \frac{G(\sigma_\phi)}{\|G(\sigma_\phi)\|_2^2 + \epsilon}, \tag{8}$$

respectively, where ϵ is a very small non-zero constant. They are the inverses of the Gaussian distortion point spread functions bounded by ϵ, which represents the Gaussian noise N_C present in the statistics. The shape of the Weiner restoration filters is shown in figure 2. In equation (6) the radial distortion is proportional to r. Thus, the size of the radial restoration filter has the same linear dependence, $\sigma_r \propto r$. The size of the radial restoration

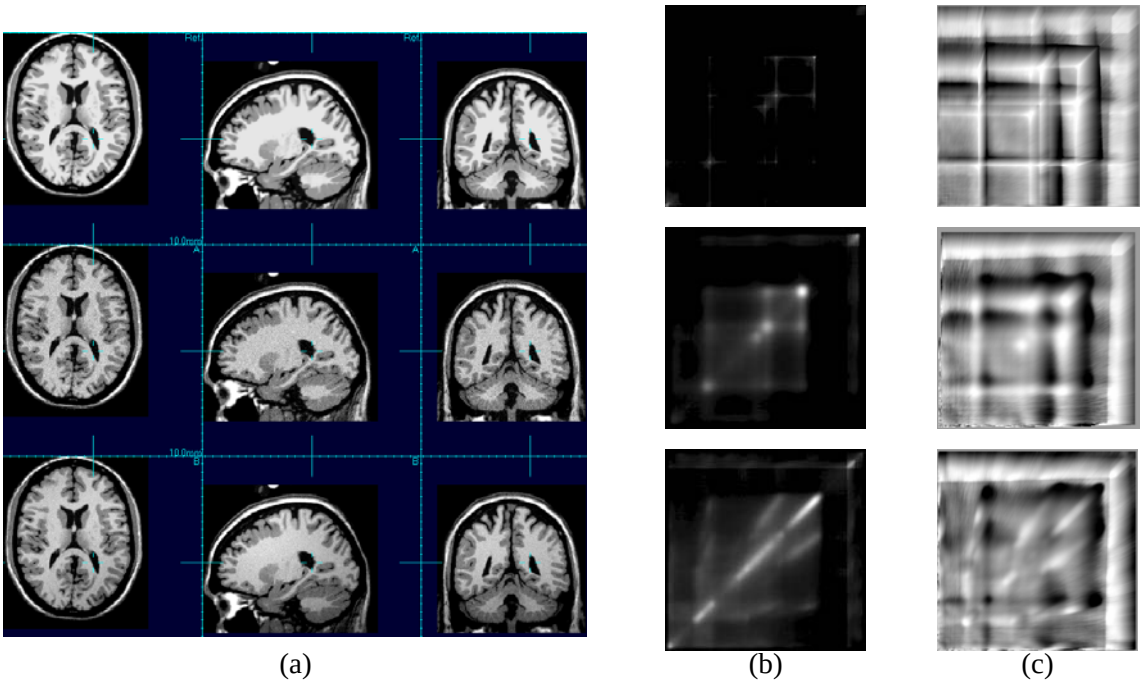

Fig. 1. Example phantom T1 images from the MNI BrainWeb. In the first row in (a) is the true phantom, in the second row is a phantom image without intensity non-uniformity but with high noise, and in the third row is a phantom with high non-uniformity and some noise. Next to each image in (b) is its co-occurrence matrix. In (c) are their corresponding restoration matrices where intensity corresponds to gain factor.

filter in the algorithm is its standard deviation normalized with respect to the dynamic range to give its normalized standard deviation:

$$\sigma_r^n = \frac{\sigma_r}{u_{max}}. \tag{9}$$

The angular restoration filter is represented in terms of angle in radians, and hence it is inherently normalized to the radius r in C_t, which is the dynamic range. The normalized standard deviation of the angular restoration filter, σ_ϕ^n, is determined from equation (7). The total Weiner restoration filter is the convolution of the two filters $f_q = f_r * f_\phi$, where $*$ is convolution, and is two-dimensional. A figure with different sizes for the non-stationary Weiner filter is shown in figure 3. It is applied to the co-occurrence matrix C_t and maps every co-occurrence (u_0, u_1) to an expected one (u_0^q, u_1^q) to give the expected restored co-occurrence matrix $C_t^q = C_t * f_q$. The restoration of the co-occurrence matrix gives a restoration matrix R_t with a gain factor for each intensity co-occurrence. The gain is the ratio of the new position u_0^q of the intensity of the central voxel over the initial position u_0 of the same intensity. Thus, the restoration factor or gain is $R_t(u_0, u_1) = u_0^q/u_0$. The co-occurrence statistics of the T1 BrainWeb phantom images in figure 1 (b) are used to compute the restoration matrices shown in figure 1 (c).

2.6. Estimation of the Spatial Non-Uniformity

The restoration matrix R_t is backprojected to the image. To this end we consider a sphere of radius ρ around a voxel $\mathbf{x}_0$. The size of this neighborhood is the same as the size of the neighborhood that was used to compute the co-occurrence statistics C_t. This sphere gives $\left(\frac{4}{3}\pi\rho^3 - 1\right)$ intensity co-occurrences with the intensity of voxel $\mathbf{x}_0$. These intensity co-occurrences are used to index the restoration matrix R_t to get an equal number of gain factors.

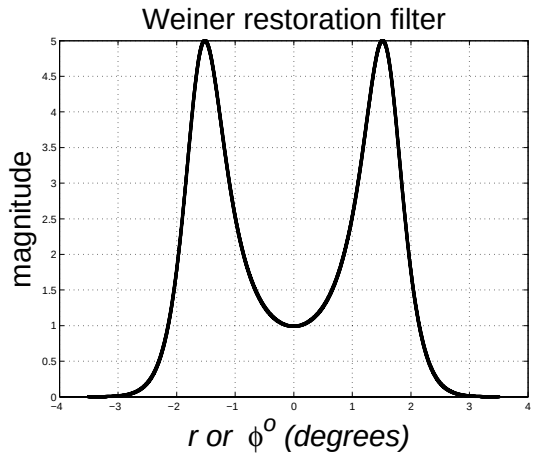

Fig. 2. The shape of the Weiner restoration filter in both the radial r and angular ϕ dimensions.

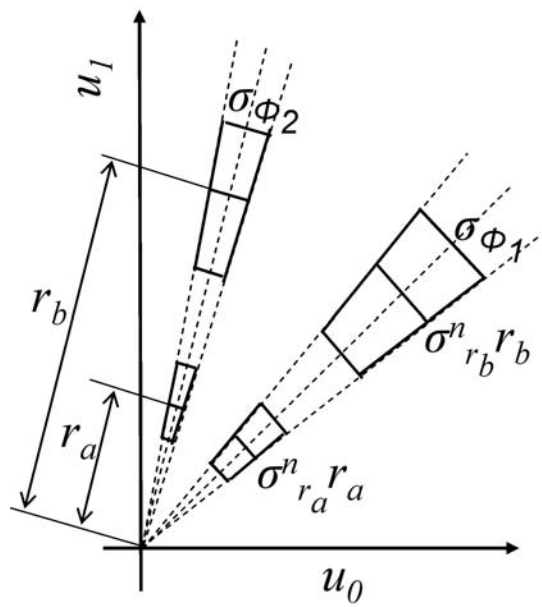

Fig. 3. The radial and angular sizes of the non-stationary Weiner restoration filter f_q change with its position on the co-occurrence matrix.

Their expected value gives a rough estimate of the restoration image W_t^{rough} at $\mathbf{x}_0$:

$$W_t^{rough}(\mathbf{x}_0) = E_{\mathbf{x}_1}(R_t(I_t(\mathbf{x}_0), I_t(\mathbf{x}_1))) = \frac{1}{\left(\frac{4}{3}\pi\rho^3 - 1\right)} \sum_{|\mathbf{x}_1 - \mathbf{x}_0| \leq \rho} R_t(I_t(\mathbf{x}_0), I_t(\mathbf{x}_1)). \tag{10}$$

The rough estimate of the spatial restoration given by this equation is the inverse of the rough estimate of the non-uniformity field $W_t^{rough}(\mathbf{x}_0) = 1/B_t^{rough}(\mathbf{x}_0)$. The non-uniformity field is assumed to be smooth. Thus, the restoration image W_t^{rough} is filtered with a spatial Gaussian filter $G(\sigma_w)$ to give $W_t^{smooth,'} = W_t^{rough} * G(\sigma_w)$. In the first row of figure 4 is a T1 BrainWeb phantom image with $B = 40\%$ and $N = 5\%$. The rough estimate of the non-uniformity in this image is in the second row of this figure. In the third row of figure 4 is a smooth estimate of the non-uniformity.

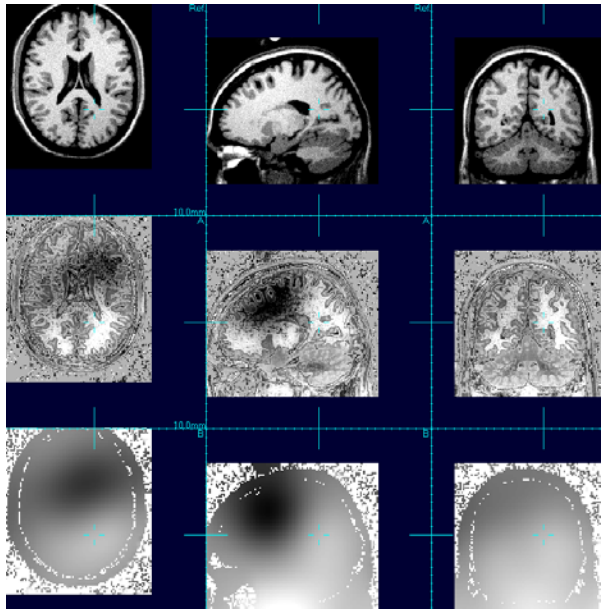

Fig. 4. The first row shows a BrainWeb phantom with both high non-uniformity $B = 40\%$ and high noise $N = 5\%$. The second row shows the rough estimate of its non-uniformity and the third row the smooth estimate of its non-uniformity.

The Weiner restoration filter contains a low-pass component to account for the noise in the statistics. As a result the filtering tends to contract the dynamic range of the image with iterations t. It is necessary to re-normalize and preserve the effective dynamic range since the normalized standard deviation of the radial restoration filter in equation (9) is a function of the maximum intensity u_{max}. The re-normalization is done using the cumulative histogram of the image I_t by rescaling the intensity range to ensure that the upper 0.9 percentile, $u^{0.9,t}$, of the cumulative histogram $\mathcal{H}_t$, $\mathcal{H}_t(u^{0.9,t}) = 0.9$ remains constant with iterations t. The correction for uniformity at iteration t is given by $W_t^{smooth} = W_t^{smooth,'} \frac{u^{0.9,0}}{u^{0.9,t}}$. This correction is applied to the restored image of iteration t pixelwise,

$$I_{t+1} = I_t \times W_t^{smooth}, \tag{11}$$

to improve its estimate. The uniformity correction is initialized at $t = 0$ to unity $W_0^{smooth} = 1, \forall \mathbf{x}$.

2.7. Condition for End of Iterations

The steps described in subsection 2.3 to subsection 2.6 are repeated iteratively. The spatial non-uniformity is assumed to have a Gaussian point spread function in its co-occurrence statistics. It follows that the Shannon entropy of the co-occurrence statistics of an image is larger than the one of the assumed corresponding true anatomic image, $S(C_{I_0}) > S(C_{I_A})$. The Shannon entropy of the co-occurrence statistics of the image decreases monotonically with iterations as a result of Weiner filtering, $S(C_{I_{t+1}}) < S(C_{I_t})$. However, the Shannon entropy of the co-occurrence statistics of an image computed over the normalized effective dynamic range, namely, the scaled entropy of the co-occurrence matrix is a non-monotonic function of the iterations t. Thus, the scaled entropy can be used directly in the stopping criterion for the iterations. In iterations t in which the scaled entropy increases $S_{sc}(C_{t+1}) > S_{sc}(C_t)$, the size of the restoration filter is halved $\sigma_{q,t+2} = \sigma_{q,t+1}/2$. The iterations end when the size of the restoration filter becomes unity, $\sigma_{q,t} = 1$ or at a maximum allowed number of iterations t_{max}. The restored image is the one whose co-occurrence matrix has minimum scaled entropy $t_{restored} = \min_{t \in [0,t_{max}]} S_{sc}(C_t)$.

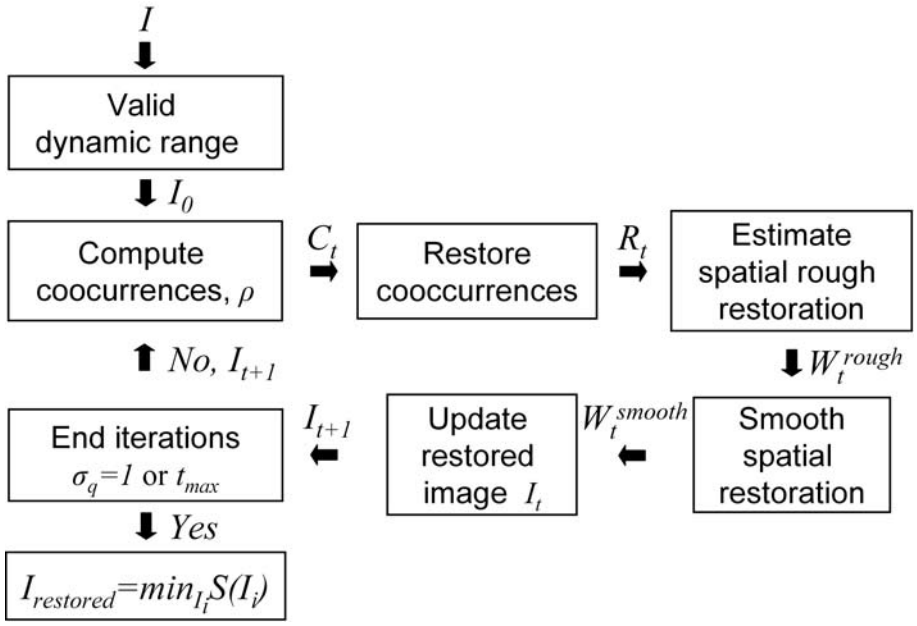

Fig. 5. A block summary of the algorithm.

2.8. Implementation and Efficiency of the Algorithm

Three of the parameters of the co-occurrence algorithm affect its performance significantly. These are the size of the Weiner filter for the restoration of the statistics σ_q^n, the size of the smoothing filter for spatial uniformity σ_w, and the size of the co-occurrence window ρ. The algorithm accepts these three significant parameters as arguments. The algorithm can also accept a foreground template that specifies the anatomical region of interest. Even though this can bring some improvement in the restoration, it was not used in this work. The algorithm is very robust to its remaining parameters that include the co-occurrence intensity resolution σ_c, the regularization for noise in the co-occurrence statistics ϵ, and t_{max}. The variation of the latter parameters and several other minor design choices can improve the efficiency of the algorithm with minimal or no loss of accuracy. The Weiner restoration filter for C_t, f_q, is separable. Its size is bounded to improve the robustness of the restoration with respect to noise and flow artifacts that can produce very high intensities. A bound on the size of the Weiner filter also avoids an unnecessary increase of the computational cost. The maximum radial size $\sigma_{r,max}$ of the filter corresponds to radial distance in C_t equal to $u^{0.9,0}$ of the histogram of the original image I_0, $\sigma_{r,max} = \sigma_r^n u^{0.9,0}$. We also set a maximum value for the size of the angular restoration filter $\sigma_{\phi,max}$ for similar reasons. It is obtained for $u^{0.9,0}$ as well as $\phi = 45°$ in C_t and a certain value of $\mu_{\nabla B}$ in equation (7). The small value of the spatial window of radius ρ for the computation of the co-occurrence statistics decreases the value of σ_ϕ^n and makes the significance of the radial standard deviation σ_r^n greater. The computation of the co-occurrence matrix C_t with the discretized version of equation (5) can be accelerated by spatially subsampling the voxels in the sphere of radius ρ either randomly or regularly in steps of Δx_1, Δx_2, and Δx_3. The same subsampling can be used to compute the rough non-uniformity correction W_t^{rough} in the discretized version of equation (10).

The rough spatial estimate for the correction of the non-uniformity is smoothed to give a smooth estimate using a spatial Gaussian pyramid [45]. The rough spatial estimate is first subsampled with a Gaussian pyramid to a fraction of its size. Subsequently, it is smoothed in the low resolution. Finally, it is upsampled with a Gaussian filter to give the smooth non-uniformity in the original resolution. During the first $t_{max}/3$ iterations the rough estimate is subsampled to 25% in each of its three dimensions x_1, x_2, and x_3. If the subsequent $t_{max}/3$ iterations

	Suggested phantom [38]	Tested for brain $4T$	Used for brain $4T$
FWHM of deconvolution	0.15	0.06,0.13,0,20	0.20
Distance of knots in space (mm)	200	20,110,200	20

Table 1. Parameters ranges tested and used for N3 to correct phantom and human brain imaging data.

are performed, the rough estimate is subsample to 50% in each of its dimensions. Finally, if the last $t_{max}/3$ iterations are performed, the rough estimate is not subsampled and is smoothed in its original resolution and size. The filter that was used to both compute the pyramid of W_t^{rough} and to smooth the non-uniformity is Gaussian, which is separable.

The algorithm can be accelerated further, however, with some loss of accuracy. The effect of the smooth non-uniformity correction W_t^{smooth} can be accentuated prior to applying it to the image in equation (11) with a multiplicative factor κ to give $I_{t+1} = I_t \times (1 + \kappa(W_t^{smooth} - 1))$. Also, the computational cost can be limited by bounding the maximum allowed number of iterations t_{max}. The algorithm was implemented in the C++ programming language and batch processing of images in a database is implemented with a Perl script.

3. EVALUATION OF THE ALGORITHM

The co-occurrence algorithm has been evaluated with phantom as well as real whole head images. We used MNI BrainWeb phantom images and the simulated $1.5T$ non-uniformities provided from the same source [44, 43]. The real images were acquired at $4T$. The difference in the field strength results in different amounts of non-uniformity in the images of the two databases. In our algorithm this was reflected by a different choice for the spatial smoothing parameter σ_w for the images of the two databases. The remaining parameters of the co-occurrence algorithm were the same for both databases. The size of the restoration filter was $\sigma_r^n = 0.026$ and $\mu_{\nabla B} = 0.3$ in equation (7). The co-occurrence statistics in equation (4) were computed in a sphere of $\rho = 9mm$ with a factor for regular subsampling of $\Delta x_1 = \Delta x_2 = \Delta x_3 = 3mm$ and the order of the statistics in the same equation was $n = 3$. The high order of co-occurrences is necessary for the restoration of whole head images. The maximum number of iterations was set to $t_{max} = 36$. The standard deviation of the Parzen window in equation (5) was $\sigma_c = 1.5$.

The co-occurrence algorithm was compared over these two databases with N3 [38], a very commonly used technique for bias field correction [5]. The least spatial decimation factor of two was used for this technique with a maximum of 1000 iterations. The remaining parameters of N3 are the FWHM of the deconvolution kernel and the distance between the knots of the spline bases. The values used for these parameters are listed in table 1. The two algorithms were evaluated for phantom images with the uncorrupted noise free and intensity uniform MNI BrainWeb head phantom. The algorithms were also evaluated with human head images using the sharpness of the histograms of the restored images that was quantified with the Shannon entropy. The experiments were performed on a Xeon processor of $3.6GHz$ and $8GB$ of RAM.

3.1. Preprocessing for the Extraction of the Signal Region in an Image

The co-occurrence algorithm was applied to whole head imaging data. A preprocessing step is used to remove the low signal regions of background and noise. The image statistics used to extract the signal region are the one dimensional diagonal self-co-occurrence statistics. The noise in these statistics corresponds to a compact distribution in the low intensity range. The noise due to acquisition in a magnitude MR image is given by a Rayleigh distribution, $P(N) \propto (u/\sigma_N^2)e^{-u^2/2\sigma_N^2}$ [46, 42], where σ_N is the standard deviation of the superimposed

	$N = 0\%$ $B = 0\%$	$N = 3\%$ $B = 40\%$	$N = 5\%$ $B = 0\%$	$N = 5\%$ $B = 20\%$	$N = 5\%$ $B = 40\%$
N3 (10^{-2})	1.40	8.17	12.76	12.56	12.77
Co-occurrence (10^{-2})	0 (-100%)	7.50 (-8.21%)	12.43 (-2.54%)	12.20 (-2.92%)	12.27 (-3.92%)

Table 2. The error is the absolute value of the difference between a restored T1 phantom image and the true T1 BrainWeb phantom. A variety of synthetic non-uniformity fields B and noise levels N were used. In all cases the error of the co-occurrence algorithm is lower. The greatest difference is that for the true intensity uniform and noise free image for which the co-occurrence algorithm has no error.

noise. This distribution is fit using the intensity and density value of the peak noise density. The fitted noise distribution is subtracted from the image statistics to give the remainder distribution. The intensity range where the noise density is higher than the remainder density gives the noise intensity range. The spatial locations that correspond to noise intensities were assigned to the background. The largest connected component of the domain with signal intensities was assigned to the signal region. The largest connected component is computed at a lower image resolution to improve efficiency. The non-uniformity is computed over the signal region and subsequently extrapolated to the low signal or no signal regions. The extrapolation is performed by numerically solving the Laplace's $\nabla B = 0$ equation over the noise domain. The boundary conditions are Dirichlet with the non-uniformity fixed over the signal region.

3.2. Phantom Images

The data used were $1.5T$ T1 BrainWeb phantom brain images corrupted by synthetic non-uniformities also provided by BrainWeb [44, 43]. The spatial smoothing of the non-uniformity in the co-occurrence algorithm was $\sigma_w = 77mm$. N3 was run with the parameters suggested for this dataset [38] given in the first column of table 1. We also computed the error maps for that data compared to the uncorrupted true phantom. Even though the restoration was performed for the whole head phantom images, the error images were computed only over the brain region. The brain region was extracted from the true uncorrupted phantom using the Brain Extraction Tool (BET) [47]. The brain region in the original as well as the restored images were normalized to zero mean and unit L_1 norm. The true minus the restored images were subsequently subtracted. The absolute value of the difference image was the error image. The L_1 norm of the error image was used as a measure of the error.

The error values for the phantom images tested are given in table 2. In all cases the error with our algorithm was lower than that of N3. The lower error demonstrates the improved performance of the co-occurrence algorithm as well as the improved stability of its stopping criterion. Two example corrections with the highest level of simulated non-uniformity used, 40%, and noise levels of 3% and 5% are shown in figures 6(a-b) and (c-d), respectively. In both examples in (b) and (d) the first row shows the original corrupted phantom with intensity non-uniformity and noise, the second row shows the restoration with N3, and the last row shows the restoration with the co-occurrence algorithm. The images are shown with their dynamic ranges windowed to those of their white matter. The N3 restoration contains a considerable residual of the intensity non-uniformity. The white matter intensity in the image restored with the co-occurrence algorithm is more uniform. The higher accuracy of the co-occurrence restoration is also shown by the error images in the same figure. The average time duration of the co-occurrence algorithm is $37min$ whereas that of N3 is $31min$.

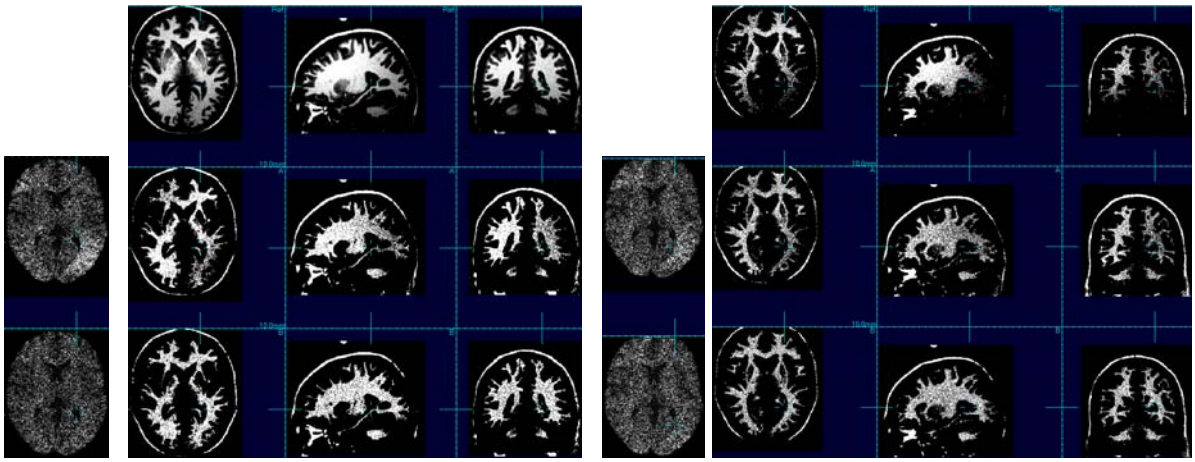

(a) (b) (c) (d)

Fig. 6. Restorations of two phantom images with non-uniformity of 40% and noise levels 3% and 5% in (a-b) and (c-d), respectively. In (b) and (d) the first row shows the original corrupted phantom, in the second row is the restoration with N3, and the third row shows the restoration with the co-occurrence algorithm. The N3 restoration contains a considerable residual of the non-uniformity. The improved performance of the co-occurrence algorithm is demonstrated by the higher uniformity of the white matter intensity. The error images of the axial sections of the restorations are shown next to the restored images in (a) and (c), respectively. The error images for the co-occurrence restorations are darker, which demonstrates improved accuracy.

3.3. Human Head Images

Human brain MRI images were acquired at $4T$ with an 8-channel array head coil. The 8-channel receiver coil had larger field non-uniformity than a conventional birdcage coil but provided better signal to noise, especially at the outer brain regions close to the coils. A T1-weighted magnetization prepared rapid gradient echo (MPRAGE) sequence was used. The parameters of the sequence were $TR/TE = 2300/3.37ms$, $TI = 950ms$, and a flip angle of $7°$. The size of the images acquired is $256 \times 256 \times 176$ voxels with a uniform voxel resolution of $1.0mm \times 1.0mm \times 1.0mm$. The algorithm was applied to head images of subjects from elderly populations. The spatial smoothing of the non-uniformity in the co-occurrence algorithm was $\sigma_w = 25mm$. N3 was run for a variety of parameters in the ranges recommended by its authors and given in the third column of table 1 [38]. The objective of N3 is to sharpen the histogram distributions. We observed the histograms and selected the parameters that gave the image that had the histogram with the most compact distributions. We also verified our selection by measuring the sharpness as a decrease in the Shannon entropy of the histogram and selected the parameter set that minimized it. The best performing parameters were $FWHM = 0.2$ and distance of $20mm$ between the knots, in the third column of table 1. The minimal entropy values are in table 3. In all test cases the entropy of the histogram of the image restored with our algorithm was lower than that of the image restored with N3 indicating that the co-occurrence algorithm provides an improvement over N3.

The corrections of four representative images are shown in figure 7. In each example the first row shows the acquired image, the second row shows the restoration with N3, and in the last row is the restoration with the co-occurrence algorithm. The images are shown with their dynamic range windowed to that of the white matter. The N3 restoration contains a considerable residual of the non-uniformity and sometimes even accentuates it. Also N3 decreases image contrast by darkening the bright white matter and introducing overshooting contours at the borders between different regions such as between gray matter and white matter at the cortex. The white matter intensity in the image restored with the co-occurrence algorithm is more uniform.

Image\ Alg.	N3	Co-occurrence
1 (nats)	4.85	4.63
2 (nats)	4.68	4.50
3 (nats)	4.46	4.30
4 (nats)	4.84	4.60
5 (nats)	4.80	4.53
6 (nats)	4.62	4.45
7 (nats)	4.85	4.53
8 (nats)	5.44	5.33
9 (nats)	4.92	4.90
10 (nats)	5.15	4.76

Table 3. Comparison between the entropies of the histograms of the restored images. In all cases the entropy of the image restored with the co-occurrence algorithm is lower than the entropy of the image corrected with N3. This is an indication of higher performance of the co-occurrence algorithm.

The human head images were from elderly populations which are particularly challenging to restore. They may have enlarged ventricles, lower contrast to noise ratio, lower cortical thickness, and many of them may have a white matter lesion load as well as some motion artifacts. They are an excellent testing ground for our algorithm. Its high performance on these images demonstrates its robustness and reliability. The duration of the restoration depends on the amount of non-uniformity present in an image. It took on average 1:23hrs with the co-occurrence algorithm and on average 2:21hrs with N3. Thus, the co-occurrence algorithm is also significantly more efficient.

4. DISCUSSION AND CONCLUSION

Most intensity uniformity restoration algorithms operate on the logarithm of the intensities. Even though this intensity transformation can make the non-uniformity additive it warps the dynamic range in a non physical way. As a result it can increase noise and decrease the contrast to noise ratio. In this work we operate on the original intensities. The image noise in magnitude MR images is given by a Rayleigh distribution [46, 42]. In this work the Rayleigh model for the noise is used during preprocessing for the extraction of the signal region. The nonunifomity estimation is performed only over the signal region where the spatial noise can be approximated as Gaussian. Similarly, the computation of the non-uniformity over the signal region allows the algorithm to assume that both the non-uniformity and noise in the co-occurrence statistices are also given by unimodal Gaussian distributions. The unimodal Gaussian distribution may not be representative for the non-uniformity, particularly in high field images. However, the restoration is robust with respect to the shape of the Weiner restoration filter and is mainly dependent on its overall variance.

Another pivotal assumption of the algorithm is that the intensity non-uniformity is spatially smooth. In spin echo sequences the non-uniformity may have abrupt variations at the borders between different tissues. However, for the purpose of image processing these abrupt changes can be absorbed into the tissue statistics [39]. The algorithm also assumes that in the intrinsic anatomic image I_A the tissue distributions are discriminable. The restoration between two regions may be problematic if the discriminability between the distributions in I_A is low or does not exist and the two regions are also spatially close. The smoothing of the initial estimate of the uniformity

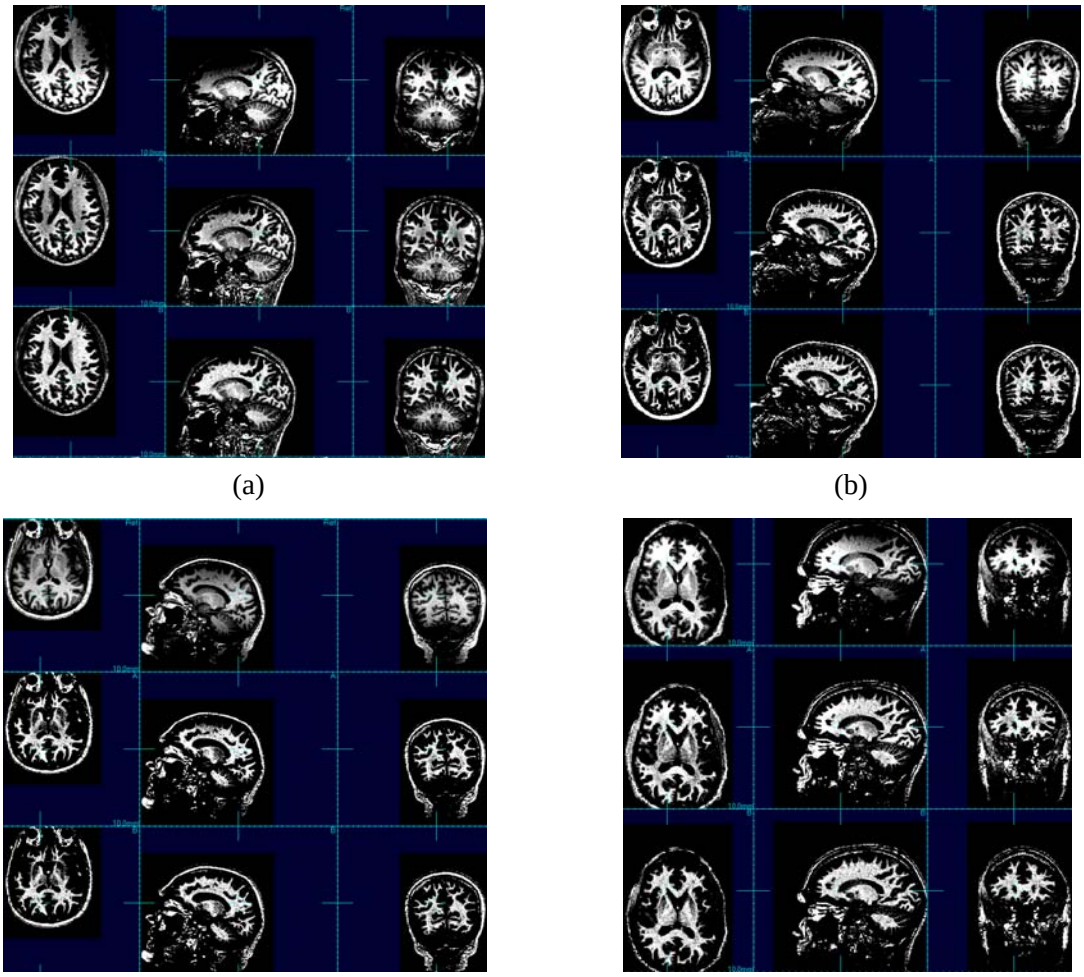

(a) (b) (c) (d)

Fig. 7. Examples of restorations of four human head images. In each example the first row shows the acquired image, the second row shows the correction with N3, and in the third row is the restoration with the co-occurrence algorithm. The N3 restoration contains a considerable residual of the non-uniformity and sometimes even accentuates it. Also, it darkens the white matter and introduces overshooting contours at the borders between different regions such as between the gray matter and the white matter regions at the cortex. The improved performance of the co-occurrence algorithm is demonstrated by the higher uniformity of the white matter intensity in these images.

correction is done with a Gaussian which has a local effect. Smoothing with more global bases such as polynomials or splines may accentuate the non-uniformity in some parts of the image.

Our algorithm was evaluated with high field human head images from elderly populations which are particularly challenging to restore. Its high performance on these images demonstrates its robustness and reliability. The algorithm is also time efficient. Its efficiency can be increased even further without loss of accuracy by taking advantage of the fact that all the steps of the algorithm are fully parallelizable. In conclusion, we developed a new algorithm that uses local intensity co-occurrences for effective image restoration from intensity non-uniformity distortion in MR images.

5. APPENDIX

5.1. Effect of Additive Image Noise on Co-Occurrence Statistics

We consider the statistics of a single contiguous tissue. The tissue is assumed to be intensity uniform and hence the variance of its statistics is assumed to be zero. As described in subsection 2.1 we also assume that the superimposed noise N is Gaussian, independently, and identically distributed with zero mean and variance Σ. Thus, the variance of the tissue distribution in the image histogram is $\Sigma_h = \Sigma$. The histogram of this tissue is compared with the one-dimensional diagonal self-co-occurrence statistics of pairs of intensities of the same contiguous tissue. The noise in different voxels is assumed to be independent, and hence the conditional co-occurrence statistics reduce to the product of the densities of the two Gaussians, one for each of the voxels of the same intensity. The product must be renormalized to give a new distribution, the product of two Gaussians distribution whose variance Σ_c is given by [48]:

$$\Sigma_c = \left(\Sigma^{-1} + \Sigma^{-1}\right)^{-1} = (2\Sigma^{-1})^{-1} = \tag{12}$$

$$= \frac{\Sigma}{2} = \frac{\Sigma_h}{2}. \tag{13}$$

Thus, the variance of a contiguous tissue distribution in the diagonal self-co-occurrence statistics is half of the distribution of the same tissue in the histogram $\Sigma_c = \Sigma_h/2$. This increases the discriminability between tissue distributions of the co-occurrences compared to those of the histogram.

In this work a number of co-occurrences with each of the voxels is considered in equation (4). This summation is a linear transformation of random variables with identical mean and variance. Hence, the variance Σ_c is not affected by the summation. The analysis in this appendix emphasizes the effect of noise in the variance and ignores the effect of spatial intensity non-uniformity. In the algorithm we minimize the effect of non-uniformity locally by selecting co-occurrences that lie within a small sphere of radius ρ. The effect of the intensity non-uniformity is examined in subsequent subsections.

5.2. Effect of Image Non-Uniformity on the Radial Dimension of the Co-Occurrence Statistics

We consider the effect of the intensity non-uniformity on a single anatomic tissue. We assume that both the distribution of the tissue and the distribution of the non-uniformity are Gaussian. The distribution of the tissue has parameters μ_A and σ_A and the distribution of the non-uniformity has parameters μ_B and σ_B. The two distributions are sampled spatially to give two images, which are multiplied to give image I. The distribution of the product image I is a normal product distribution, which for two factors is a modified Bessel function of the second kind P_I [49]. The moment generating function of this distribution gives [50]:

$$E(P_I) = \mu_B\mu_A + \rho\sigma_B\sigma_A, \tag{14}$$

and

$$V(P_I) = \mu_B^2\sigma_A^2 + \mu_A^2\sigma_B^2 + \sigma_B^2\sigma_A^2 + 2\rho\mu_B\mu_A\sigma_B\sigma_A + \rho^2\sigma_B^2\sigma_A^2. \tag{15}$$

We assume that the spatial samples of the two Gaussian distributions of anatomy and of non-uniformity are uncorrelated with $\rho = 0$. This assumption simplifies the expression for the variance in equation (15) to:

$$V(P_I) = \mu_B^2\sigma_A^2 + \mu_A^2\sigma_B^2 + \sigma_B^2\sigma_A^2. \tag{16}$$

For a specific value of anatomic intensity u_A the variance of the total distribution is $V(Y|u_A) = u_A^2\sigma_B^2$. Its square root gives:

$$\sigma(P_I|u_A) = u_A\sigma_B. \tag{17}$$

This relation holds for each of the two axes in the co-occurrence statistics. Consider a co-occurrence between intensities u_{A_0} and u_{A_1}. The geometry in Figure 8 shows that:

$$\sigma(C|u_{A_0}, u_{A_1}) \propto \sigma_B \sqrt{u_{A_0}^2 + u_{A_1}^2} = \sigma_B r, \tag{18}$$

where r is the distance of a co-occurrence from the origin.

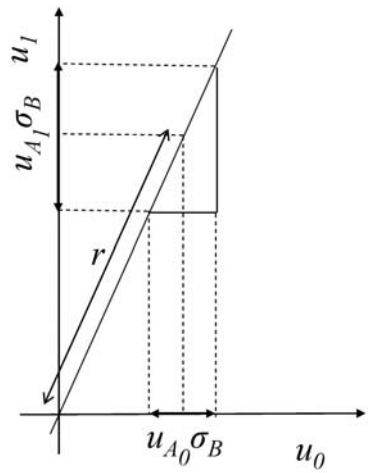

Fig. 8. Radial standard deviation of a tissue distribution due to intensity non-unifomity.

5.3. Effect of Image Non-Uniformity on the Angular Dimension of the Co-occurrence Statistics

As shown in appendix 5.2 the zero order term $B(\mathbf{x}_0)$ of the expansion of the field of the non-uniformity locally causes only a radial deviation of the co-occurrences in C_t. We consider the angular deviation caused by the first order term $\nabla B(\mathbf{x}_0)$ and ignore higher order terms. Thus, the intensity of the central pixel is not affected and a co-occurrence (u_0, u_1) is mapped to $(u_0, u_1 + \Delta u_1)$.

The cosine law for angle $\Delta\phi$ over triangle ABD gives the cosine of the angle as a function of u_0, u_1, and Δu_1:

$$\Delta u_1^2 \quad = \quad (u_0^2 + u_1^2) + (u_0^2 + (u_1 + \Delta u_1)^2) - 2\sqrt{u_0^2 + u_1^2}\sqrt{u_0^2 + (u_1 + \Delta u_1)^2}\cos\Delta\phi \Rightarrow \tag{19}$$

Line BC of length ν forms the isosceles triangle ABC. The cosine law for that triangle gives:

$$\nu^2 = 2(u_0^2 + u_1^2) - 2(u_0^2 + u_1^2)\cos\Delta\phi. \tag{20}$$

The cosine $\cos\Delta\phi$ can be eliminated from equation (19) and equation (20) to give

$$\nu^2 \quad = \quad 2(u_0^2 + u_1^2) - 2(u_0^2 + u_1^2)\frac{\Delta u_1^2 - 2u_0^2 - 2u_1^2 - \Delta u_1^2 - 2u_1\Delta u_1}{-2\sqrt{u_0^2 + u_1^2}\sqrt{u_0^2 + u_1^2 + \Delta u_1^2 + 2u_1\Delta u_1}}. \tag{21}$$

The substitution $\Delta u_1 = \alpha u_1$ in this equation, where $\alpha = \nabla B$ gives

$$\nu^2 \quad = \quad 2(u_0^2 + u_1^2)\left[1 - \frac{u_0^2 + (1+\alpha)u_1^2}{\sqrt{u_0^2 + u_1^2}\sqrt{u_0^2 + u_1^2(1+\alpha)^2}}\right]. \tag{22}$$

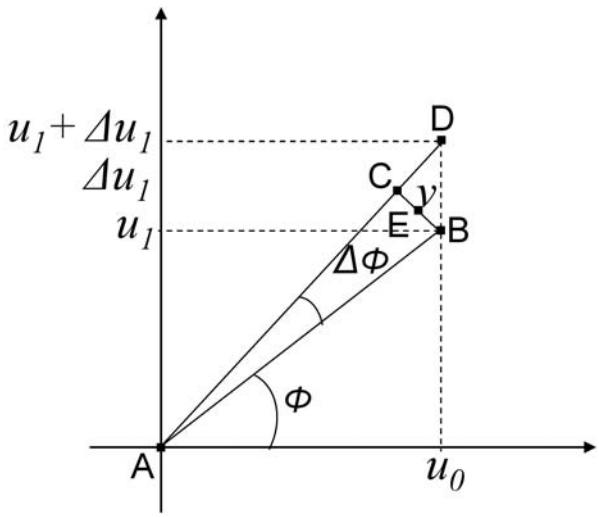

(a) An intensity pair (u_0, u_1) as a result of the non-uniformity gradient $\alpha = \nabla B$ becomes $(u_0, u_1(1+\alpha))$. The angle ϕ of (u_0, u_1) with the horizontal axis becomes $\phi + \Delta\phi$.

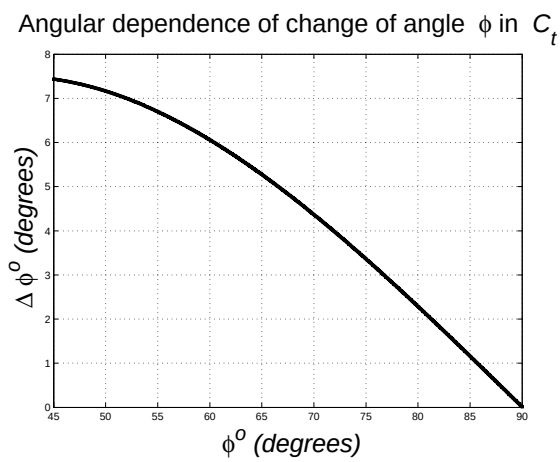

(b) The effect of a constant non-uniformity $\alpha = 0.3$ on the rotational angle $\Delta\phi$ as a function of the angle ϕ. The effect on co-occurrences close to the diagonal $\phi = 45°$ is the highest.

Fig. 9. The effect of non-uniformity on the angular size of the Weiner restoration filter.

The substitution $\tan\phi = u_1/u_0$ in equation (22) gives:

$$\frac{\nu^2}{4(u_0^2+u_1^2)} = \frac{1}{2}\left[1 - \frac{1+\tan^2\phi(1+\alpha)}{\sqrt{1+\tan^2\phi}\sqrt{1+\tan^2\phi(1+\alpha)^2}}\right]. \tag{23}$$

The midpoint E of line segment BC gives the right triangle ABE with $\sin\frac{\Delta\phi}{2} = \frac{\nu}{2\sqrt{u_0^2+u_1^2}}$. This can be substituted in equation (23) above to give

$$\sin^2\frac{\Delta\phi(\phi,\nabla B)}{2} = \frac{1}{2}\left[1 - \frac{1+\tan^2\phi(1+\alpha)}{\sqrt{1+\tan^2\phi}\sqrt{1+\tan^2\phi(1+\alpha)^2}}\right]. \tag{24}$$

In this equation we assume that the mean value of the gradient $\mu_{\nabla B} = \overline{\nabla B(\mathbf{x}_0)}$ for α gives the standard deviation $\Delta\phi(\phi,\alpha) = \sigma_\phi$ of the unimodal Gaussian point spread function $G(\sigma_\phi)$ to get equation (7) in subsection 2.3.

6. REFERENCES

[1] J.G. Sled and G.B. Pike, "Standing-wave and RF penetration artifacts caused by elliptic geometry: An electrodynamic analysis of MRI," *IEEE Transactions on Medical Imaging*, vol. 17, no. 4, pp. 653–662, 1998.

[2] R. Stollberger and P. Wach, "Imaging of the active B1 field in vivo," *Magnetic Resonance in Medicine*, vol. 35, pp. 246–251, 1996.

[3] E.D. Vita, D.L. Thomas, R. Deichmann, R. Turner, and R.J. Oldidge, "Fast B1 mapping with EPI," in *Proc. of ISMRM*, 2004, vol. 11.

[4] L. Axel, J. Costantini, and J. Listerud, "Intensity correction in surface-coil MR imaging," *Am. J. Roentgenology*, vol. 148, pp. 418–420, 1987.

[5] J. Arnold, J.S. Liow, K.A. Schaper, J.J. Stern, J.G. Sled, D.W. Shattuck, A.J. Worth, M.S. Cohen, R.M. Leahy, J.C. Mazziota, and D.A. Rottenberg, "Qualitative and quantitative evaluation of six algorithms for correcting intensity nonuniformity effects," *Neuroimage*, vol. 13, pp. 931–943, 2001.

[6] B. Belaroussi, J. Milles, S. Carme, Y.M. Zhu, and H.B. Cattin, "Intensity non-uniformity correction in MRI: Existing methods and their validation," *Medical Image Analysis*, vol. 10, pp. 234–246, 2006.

[7] Z. Hou, "A review on MR image intensity inhomogeneity correction," *International Journal of Biomedical Imaging*, vol. 2006, no. 49515, pp. 1–11.

[8] U. Vovk, F.Pernus, and B. Likar, "A review of methods for correction of intensity inhomogeneity in MRI," *IEEE Transactions on Medical Imaging*, vol. 26, no. 3, pp. 405–421, 2007.

[9] R. Guillemaud and M. Brady, "Estimating the bias field of MR images," *IEEE Transactions on Medical Imaging*, vol. 16, pp. 238–251, 1997.

[10] K.V. Leemput, F. Maes, D. Vandermeulen, and P. Suetens, "Automated model based bias field correction of MR images of the brain," *IEEE Transactions on Medical Imaging*, vol. 18, no. 10, pp. 885–896, 1999.

[11] Y. Zhang, M. Brady, and S. Smith, "Segmentation of brain MR images through a hidden Markov random field model and the expectation-maximization algorithm," *IEEE Transactions on Medical Imaging*, vol. 20, no. 1, pp. 45–57, 2001.

[12] B.H. Brinkmann, A. Manduca, and R.A. Robb, "Optimized homomorphic unsharp masking for MR grayscale intensity correction," *IEEE Transactions on Medical Imaging*, vol. 17, no. 2, pp. 161–171, 1998.

[13] M. Cohen, R. DuBois, and M. Zeineh, "Rapid and effective correction of RF inhomogeneity for high field magnetic resonance imaging," in *Proc. of Human Brain Mapping*, 2000, vol. 10, pp. 204–211.

[14] C. DeCarli, D.G.M. Murphy, D. Teichberg, G. Campbell, and G.S. Sobering, "Local histogram correction of MRI spatially dependent image pixel intensity nonuniformity," *Journal of Magnetic Resonance Imaging*, vol. 6, pp. 519–528, 1996.

[15] C. Studholme, V. Cardenas, E. Song, F. Ezekiel, A. Maudsley, and M. Weiner, "Accurate template based correction of brain MRI intensity distortion with application to dementia and aging," *IEEE Transactions on Medical Imaging*, vol. 23, no. 1, pp. 99–110, 2004.

[16] K.M. Pohl, W.M. Wells, A. Guimond, K. Kasai, M.E. Shenton, R. Kikinis, W.E.L. Grimson, and S.K. Warfield, "Incorporating nonrigid registration into expectation maximization algorithm to segment MR images," in *Proc. of MICCAI*, 2002.

[17] B. Dawant, A. Zijdenbos, and R. Margolin, "Correction of intensity variations in MR images for computer aided tissue classification," *IEEE Transactions on Medical Imaging*, vol. 12, no. 4, pp. 770–781, 1993.

[18] W.M. Wells, W.E.L. Grimson, R. Kikinis, and F.A. Jolesz, "Adaptive segmentation of MRI data," *IEEE Transactions on Medical Imaging*, vol. 15, pp. 429–442, 1996.

[19] K. Held, E.R. Korps, B.J. Krause, W.M. WellsIII, R. Kikinis, and H.-W. Muller Gartner, "Markov random field segmentation of brain MR images," *IEEE Transactions on Medical Imaging*, vol. 16, pp. 878–886, 1997.

[20] M. Styner, C. Brechbuhler, G. Szekely, and G. Gerig, "Parametric estimate of intensity inhomogeneities applied to MRI," *IEEE Transactions on Medical Imaging*, vol. 19, no. 3, pp. 153–165, 2000.

[21] C.R. Meyer, P.H. Bland, and J.Pipe, "Retrospective correction of intensity inhomogeneities in MRI," *IEEE Transactions on Medical Imaging*, vol. 14, no. 1, pp. 36–41, 1995.

[22] S. Prima, N. Ayache, T. Barrick, and N. Roberts, "Maximum likelihood estimation of the bias field in MR brain images: Investigating different modelings of the imaging process," in *Proc. of MICCAI*, 2001, vol. 2208, pp. 811–819.

[23] A.P. Dempster, N.M. Laird, and D.B. Rubin, "Maximum likelihood from incomplete data via the EM algorithm (with discussion)," *Journal of the Royal Statistical Society B*, vol. 39, pp. 1–38, 1977.

[24] A. Ashburner and K.J. Friston, "Voxel-based morphometry–the methods," *Neuroimage*, vol. 11, pp. 805–821, 2000.

[25] D. Pham and J. Prince, "An adaptive fuzzy c-means algorithm for image segmentation in the presence of intensity inhomogeneities," *Pattern Recognition Letters*, vol. 20, pp. 57–68, 1999.

[26] M.N. Ahmed, S.M. Yamany, N. Mohamed, A.A. Farag, and T. Moriarty, "A modified fuzzy c-means algorithm for bias field estimation and segmentation of MRI data," *IEEE Transactions on Medical Imaging*, vol. 21, no. 3, pp. 193–199, 2002.

[27] S. Gilles, M. Brady, J. Declerck, J.P. Thirion, and N. Ayache, "Bias field correction of breast MR images," in *Proc. of the 4th International Conference on Visualization in Biomedical Computing*, 1996, vol. 1131, pp. 153 – 158.

[28] S.L. Lee and M.W. Vannier, "Post-acquisition correction of MR inhomogeneities," *Magnetic Resonance in Medicine*, vol. 36, pp. 275–286, 1996.

[29] R. Kimmel, M. Elad, D. Shaked, R. Keshet, and I. Sobel, "A variational framework for retinex," *International Journal of Computer Vision*, vol. 52, no. 1, pp. 7–23, 2003.

[30] D.H. Brainard and B.A. Wandell, "Analysis of the retinex theory of color vision," *Journal of the Optical Society of America A*, vol. 3, no. 10, pp. 1651–1661, 1986.

[31] H.K. RisingIII, "Analysis and generalization of retinex by recasting the algorithm in wavelets," *Journal of Electronic Imaging*, vol. 13, no. 1, pp. 93–99, 2004.

[32] C. Han, T. Hatsukami, and C. Yuan, "A multi-scale method for automatic correction of intensity non-uniformity in MR images," *Journal of Magnetic Resonance Imaging*, vol. 13, pp. 428–436, 2001.

[33] E. Vokurka, N. Thacker, and A. Jackson, "A fast model independent method for automatic correction of intensity nonuniformity in MRI data," *Journal of Magnetic Resonance Imaging*, vol. 10, pp. 550–562, 1999.

[34] S. Lai and M. Fang, "A new variational shape-from-orientation approach to correcting intensity inhomogeneities in magnetic resonance images," *Medical Image Analysis*, vol. 3, no. 4, pp. 409–424, 1999.

[35] J. Luo, Y. Zhu, P. Clarysse, and I. Magnin, "Correction of bias field in MR images using singularity function analysis," *IEEE Transactions on Medical Imaging*, vol. 24, no. 8, pp. 1067–1085, 2005.

[36] U. Vovk, F. Pernus, and B. Likar, "MRI intensity inhomogeneity correction by combining intensity and spatial information," *Institute of Physics Publishing*, vol. 49, pp. 4119–4133, 2004.

[37] B. Likar, M. Viergever, and F. Pernus, "Retrospective correction of MR intensity inhomogeneity by information minimization," *IEEE Transactions on Medical Imaging*, vol. 20, no. 12, pp. 1398–1410, 2001.

[38] J. Sled, A. Zijdenbos, and A. Evans, "A nonparametric method for automatic correction of intensity nonuniformity in MRI data," *IEEE Transactions on Medical Imaging*, vol. 17, no. 1, pp. 87–97, 1998.

[39] J. Mangin, "Entropy minimization for automatic correction of intensity nonuniformity," *Proc. of IEEE workshop on MMBIA*, pp. 162–169, 2000.

[40] R. Bansal, L. Staib, and B.S. Peterson, "Correcting nonuniformities in MRI intensities using entropy minimization based on an elastic model," in *Proc. of MICCAI*, 2004.

[41] S. Hadjidemetriou, C. Studholme, S. Mueller, M. Weiner, and N. Schuff, "Restoration of MRI data for field nonuniformities using high order neighborhood statistics," in *Proc. of SPIE Medical Image Processing*, 2007, vol. 6512.

[42] H. Gudbjartsson and S. Patz, "The Rician distribution of noisy MRI data," *Magnetic Resonance in Medicine*, vol. 34, pp. 910–914, 1995.

[43] C.A. Cocosco, V. Kollokian, R.K.-S. Kwan, and A.C. Evans, "BrainWeb: Online interface to a 3D MRI simulated brain database," *NeuroImage*, vol. 5, no. 4-2/4, pp. S425, 1997.

[44] D.L. Collins, A.P. Zijdenbos, V. Kollokian, J.G. Sled, N.J. Kabani, C.J. Holmes, and A.C. Evans, "Design and construction of a realistic digital brain phantom," *IEEE Transactions on Medical Imaging*, vol. 17, no. 3, pp. 463–468, 1998.

[45] P. Burt and E.H. Adelson, "The Laplacian pyramid as a compact image code," *IEEE Transactions on Communication*, vol. COM-31, pp. 532–540, 1983.

[46] S.O. Rice, "Mathematical analysis of random noise," *Bell System Technical Journal*, vol. 24, pp. 100–103, 1945.

[47] S.M. Smith, "Fast robust automated brain extraction," in *Proc. of Human Brain Mapping*, 3 2002, vol. 17, pp. 143–55.

[48] M.J.F. Gales and S.S. Airey, "Product of Gaussians for speech recognition," *Computer Speech and Language*, vol. 20, pp. 22–40, 2005.

[49] E. Weisstein, *Normal Product Distribution*, MathWorld, http://mathworld.wolfram.com/ NormalProductDistribution.html.

[50] R. Ware and F. Lad, "Approximating the distribution for sums of products of normal variables," *Research report, University of Caterbury*, UCDMS 2003/15.